

tion in the accretion disk before the accretion of UOC and CC parent bodies. In the later scenario, chondrites would be enriched in chondrules formed shortly before accretion (which was constrained for H4 UOC at $^{26}\text{Al}/^{27}\text{Al} \approx 2 \times 10^{-7}$ from the metamorphic cooling of the parent body) (24). Although there is no evidence to favor one of these two extreme hypotheses over the other, it is obvious from the Al-rich chondrule that its precursors were extracted from the nebula $\sim 0.87^{+0.19}_{-0.16}$ My after CAIs and that they remained isolated in the nebula for up to ~ 3 My before chondrule formation. The presence of chondrules of different origins and different ages in the same few cubic centimeters of Semarkona is consistent with astrophysical models of the disk. Radial mixing by turbulence can efficiently distribute solids within 10 astronomical units in several tens of thousands of years, as long as these solids are small (millimeter or centimeter size) and are coupled to the gas (25), but the rate of destruction of these solids by accretion either by the Sun or by forming planetesimals is unknown. The observed age distribution (Fig. 3) does not exclude an early intense period (~ 1 My after CAIs or even before) of chondrule formation (or extraction of chondrule precursors), as was suggested by high $^{26}\text{Al}/^{27}\text{Al}$ inferred from bulk analyses of chondrules (26–28).

Our results imply the following: (i) that ^{26}Al was efficiently homogenized (within $\sim \pm 10\%$) in the inner solar system, (ii) that no substantial ^{26}Al (in excess of $^{26}\text{Al}/^{27}\text{Al} = 5 \times 10^{-5}$) was produced in the disk after time “zero” as defined by the bulk isochron of CAIs, and (iii) that the ^{26}Al – ^{26}Mg systematic has a chronological significance. Nebular models do predict an efficient

homogenization of ^{26}Al at $\sim \pm 10\%$ in the case of an external seeding of the accretion disk with ^{26}Al injected by a nearby supernova (29). In the case of the production of ^{26}Al by irradiation, it is not clear that such a level of homogeneity can be reached, unless most of the irradiated material is evaporated before time zero.

References and Notes

- G. J. Macpherson, A. M. Davis, E. K. Zinner, *Meteoritics* **30**, 365 (1995).
- B. Jacobsen *et al.*, *Earth Planet. Sci. Lett.* **272**, 353 (2008).
- K. Thrane, M. Bizzarro, J. A. Baker, *Astrophys. J.* **646**, L159 (2006).
- T. Kunihiro, A. E. Rubin, K. D. McKeegan, J. T. Wasson, *Geochim. Cosmochim. Acta* **68**, 2947 (2004).
- K. Nagashima, A. N. Krot, M. Chaussidon, *Meteorit. Planet. Sci.* **42**, A115 (2007).
- N. Sugiura, A. N. Krot, *Meteorit. Planet. Sci.* **42**, 1183 (2007).
- E. Kurahashi, N. T. Kita, H. Nagahara, Y. Morishita, *Geochim. Cosmochim. Acta* **72**, 3865 (2008).
- I. D. Hutcheon, R. Hutchison, *Nature* **337**, 238 (1989).
- S. S. Russell, G. Srinivasan, G. R. Huss, G. J. Wasserburg, G. J. MacPherson, *Science* **273**, 757 (1996).
- N. T. Kita, H. Nagahara, S. Togashi, Y. Morishita, *Geochim. Cosmochim. Acta* **64**, 3913 (2000).
- S. Mostefaoui *et al.*, *Meteorit. Planet. Sci.* **37**, 421 (2002).
- N. G. Rudraswami, J. N. Goswami, B. Chattopadhyay, S. K. Sengupta, A. P. Thapliyal, *Earth Planet. Sci. Lett.* **274**, 93 (2008).
- Materials and methods are available as supporting material on Science Online.
- G. Libourel, A. N. Krot, *Earth Planet. Sci. Lett.* **254**, 1 (2007).
- M. Chaussidon, G. Libourel, A. N. Krot, *Geochim. Cosmochim. Acta* **72**, 1924 (2008).
- M. Chaussidon, M. Gounelle, *C. R. Geosci.* **339**, 872 (2007).
- E. D. Young *et al.*, *Science* **308**, 223 (2005).
- M.-C. Liu, K. D. McKeegan, A. M. Davis, *Lunar Planet. Sci. XXXVII*, 2428 (2006).
- H. Nagahara, N. T. Kita, K. Ozawa, Y. Morishita, *Geochim. Cosmochim. Acta* **72**, 1442 (2008).
- Y. Amelin, A. N. Krot, I. D. Hutcheon, A. A. Ulyanov, *Science* **297**, 1678 (2002).
- A. N. Krot, Y. Amelin, P. Cassen, A. Meibom, *Nature* **436**, 989 (2005).
- A. Bouvier *et al.*, *Geochim. Cosmochim. Acta* **71**, 1583 (2007).
- Y. Amelin, A. Krot, *Meteorit. Planet. Sci.* **42**, 1321 (2007).
- E. Zinner, C. Gopel, *Meteoritics* **27**, 311 (1995).
- D. Bockelee-Morvan, D. Gautier, F. Hersant, J. M. Hure, F. Robert, *Astron. Astrophys.* **384**, 1107 (2002).
- A. Galy, E. D. Young, R. D. Ash, R. K. O’Nions, *Science* **290**, 1751 (2000).
- M. Bizzarro, J. A. Baker, H. Haack, *Nature* **431**, 275 (2004).
- M. Bizzarro, J. A. Baker, H. Haack, *Nature* **435**, 1280 (2005).
- A. P. Boss, *Astrophys. J.* **660**, 1707 (2007).
- K. Lodders, *Astrophys. J.* **591**, 1220 (2003).
- We gratefully thank C. Rollion-Bard, D. Mangin, and M. Champenois for their implication and expertise in ion probe techniques; J. Ravaux and A. Kohler for their help with SEM analysis; and J. Marin and P. Burnard for their attentive rereading. Constructive comments by three anonymous reviewers and fruitful discussions with F. Robert and M. Gounelle were highly appreciated and greatly improved this manuscript. This work was funded by L’Agence Nationale de la Recherche grant ANR-08-BLAN-0260-02 T-Tauri, Chem, and European Research Council grant ERC 226846 Cosmochemical Exploration of the first two Million Years of the Solar System (CEMYSS). This is CRPG publication number 2001.

Supporting Online Material

www.sciencemag.org/cgi/content/full/325/5943/985/DC1
Materials and Methods
Figs. S1 to S5
Tables S1 to S2
References

23 March 2009; accepted 19 June 2009
10.1126/science.1173907

Adjoint Tomography of the Southern California Crust

Carl Tape,^{1*} Qinya Liu,² Alessia Maggi,³ Jeroen Tromp⁴

Using an inversion strategy based on adjoint methods, we developed a three-dimensional seismological model of the southern California crust. The resulting model involved 16 tomographic iterations, which required 6800 wavefield simulations and a total of 0.8 million central processing unit hours. The new crustal model reveals strong heterogeneity, including local changes of $\pm 30\%$ with respect to the initial three-dimensional model provided by the Southern California Earthquake Center. The model illuminates shallow features such as sedimentary basins and compositional contrasts across faults. It also reveals crustal features at depth that aid in the tectonic reconstruction of southern California, such as subduction-captured oceanic crustal fragments. The new model enables more realistic and accurate assessments of seismic hazard.

The objective of seismic tomography is to produce detailed three-dimensional (3D) images of Earth’s interior by minimizing the differences between simulated (or “synthetic”) seismograms and recorded (or “observed”) seismograms. Seismic tomography has been successful in producing images of Earth’s interior, such

as large-scale variations in the mantle (1, 2), subducting slabs (3), and mantle plumes (4). These tomographic studies adopt a simple 1D (layered) reference model (5), which allows for computationally inexpensive procedures within the minimization problem. Highly accurate numerical methods, such as the spectral-element method

(SEM), may now be used to compute synthetic seismograms at regional and global scales, allowing tomographers to start the minimization procedure with more realistic 3D initial models and simulations (6–9). We demonstrated in this study that these numerical methods may be exploited within the minimization problem by using adjoint methods (10–12). We refer to this procedure as “adjoint tomography” (13).

Southern California provides an excellent setting for the two-fold objective of fitting seismograms and characterizing the crust. The station coverage (fig. S2A), especially in the Los Angeles region, is one of the densest in the world. A detailed 3D seismological model of the southern California crust has been constructed from a

¹Seismological Laboratory, California Institute of Technology, Pasadena, CA 91125, USA. ²Department of Physics, University of Toronto, Ontario M5S 1A7, Canada. ³Institut de Physique du Globe, Université de Strasbourg, 67084 Strasbourg, France. ⁴Department of Geosciences and Program in Applied and Computational Mathematics, Princeton University, Princeton, NJ 08544, USA.

*To whom correspondence should be addressed. E-mail: carltape@gps.caltech.edu

variety of seismic data sets (15). Several different approaches have been used to determine earthquake source parameters (16). Finally, an accurate wave propagation code, using the SEM, has been applied to simulate seismic wave propagation in the region (15), with recent modifications to facilitate an inverse problem (17).

We wanted to use an initial seismological Earth model that produces the maximum number of measurements for a given set of earthquakes. Hence, we began with a 3D model (14, 15) rather than a standard 1D layered model for southern California. The initial model was provided by the Southern California Earthquake Center

(SCEC) and contains results from several different data sets: seismic reflection and industry well-log data to constrain the geometry and structure of major basins, receiver function data to estimate the depth to the Mohorovicic discontinuity (Moho), and local earthquake data to obtain the 3D background wave-speed structure. The model is described in terms of shear wave speed (V_S) and bulk sound speed (V_B), which can be combined to compute compressional wave speed, $V_P^2 = (4/3)V_S^2 + V_B^2$. We extended the simulation region of (15) westward, so as to include the Coast Ranges (fig. S1). We also implemented a more recent version of the background model

(18, 19), and we obtained density (ρ) by empirically scaling V_P (20). Topography and bathymetry are included, and stations in the simulations are situated at their proper elevations.

In our inversion method, we measured frequency-dependent travel-time differences between simulated and recorded seismic waveforms (16, 21). This involves measuring both body waves and surface waves on all three components (vertical, radial, and transverse), whenever possible. The inversion required examination of 52,000 three-component seismograms of 143 crustal earthquakes. We use an adjoint method to compute the gradient of the misfit function to obtain each update to the tomo-

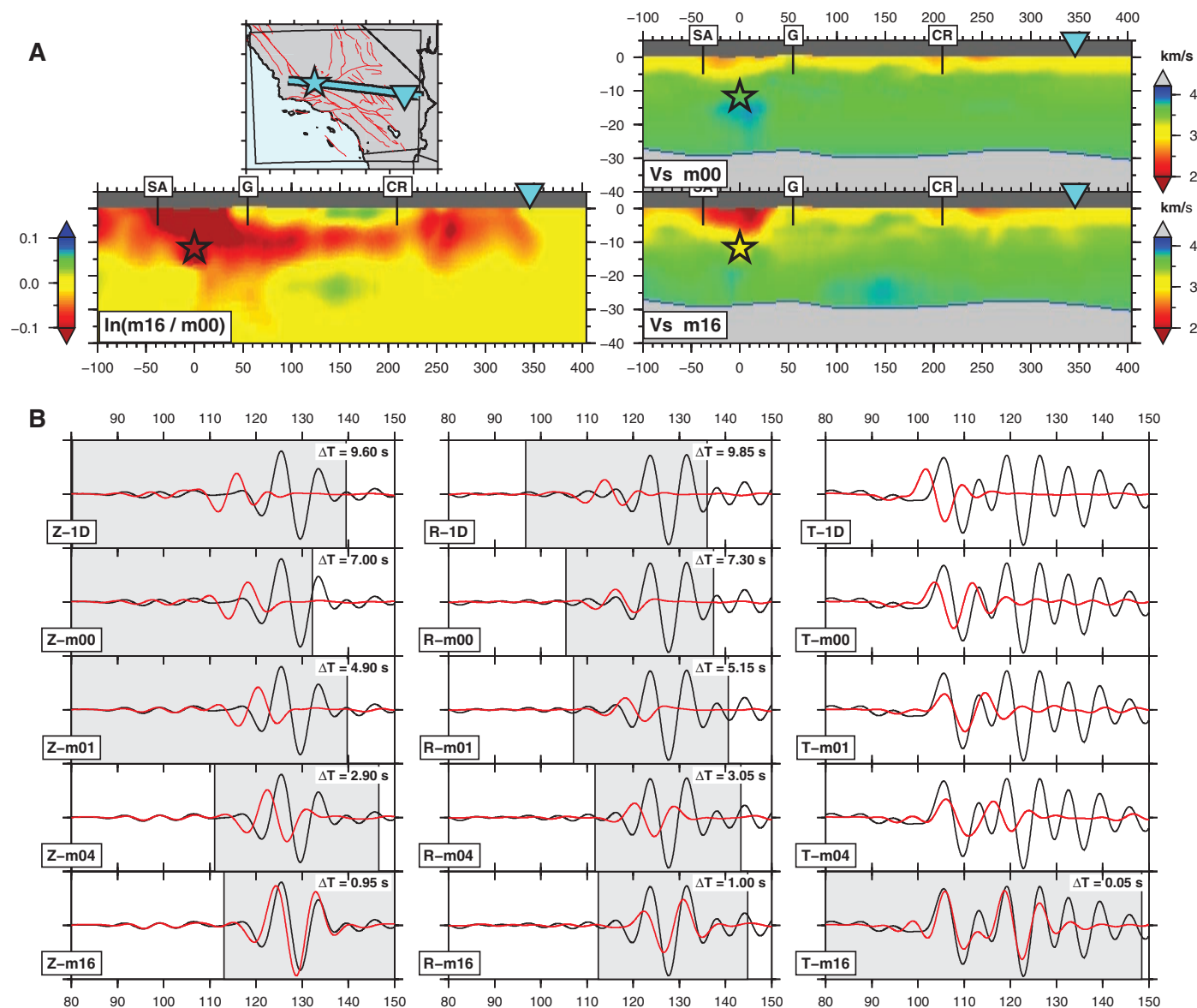


Fig. 1. Iterative improvement of a three-component seismogram. (A) Cross section of the V_S tomographic models for a path from a M_w 4.5 earthquake (stars) on the White Wolf fault to station DAN (triangles) in the eastern Mojave Desert. Vertical exaggeration is 3.0. Upper right is the initial 3D model, m_{00} ; lower right is the final 3D model, m_{16} ; and lower left is the difference between the two, $\ln(m_{16}/m_{00})$. Faults labeled for reference are San Andreas (SA), Garlock (G), and Camp Rock (CR). (B) Iterative three-component seismogram

fits to data for models m_{00} , m_{01} , m_{04} , and m_{16} . Also shown are synthetic seismograms computed for a standard 1D model (table S1). Synthetic seismograms (red) and recorded seismograms (black), filtered over the period range 6 to 30 s. Left column, vertical component (Z); center column, radial component (R); right column, transverse component (T). Inset " ΔT " label indicates the time shift between the two windowed records that provides the maximum cross-correlation (16, 21).

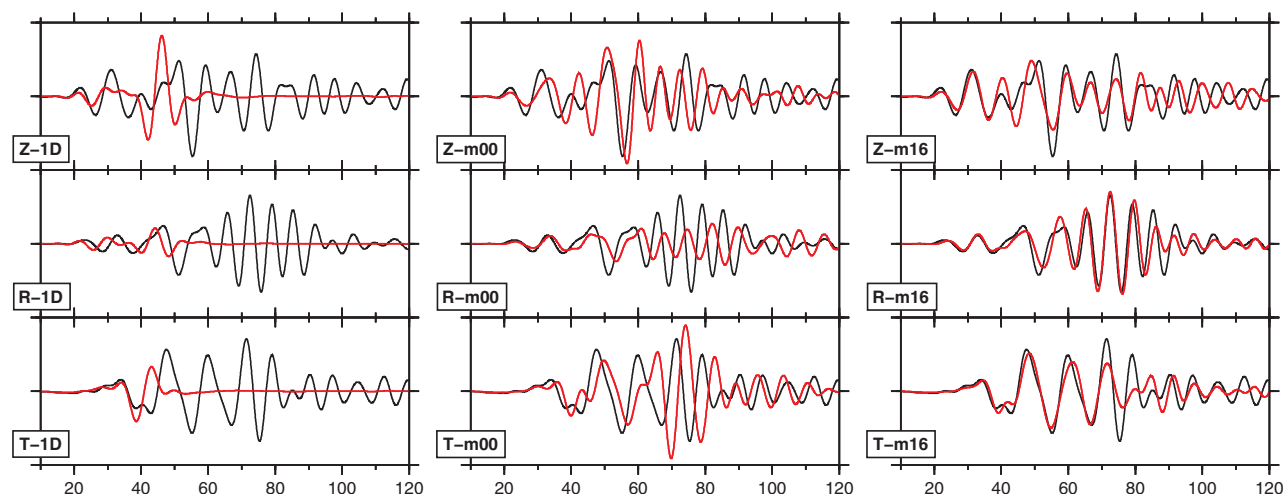


Fig. 2. Synthetic seismograms (red) and recorded seismograms (black) for the period range 6 to 30 s for a path from an earthquake beneath Chino Hills (M_w 5.4, depth 14.2 km), east of the Los Angeles basin, to station STC.CI (distance 137.1 km), within the Ventura basin. Synthetic seismograms are generated

using a 1D layered model, the initial 3D model (\mathbf{m}_{00}), and the final 3D model (\mathbf{m}_{16}) for all three components: vertical (Z), radial (R), and transverse (T). This earthquake was not used in the tomographic inversion, i.e., it is one of the “extra” earthquakes analyzed in Fig. 3.

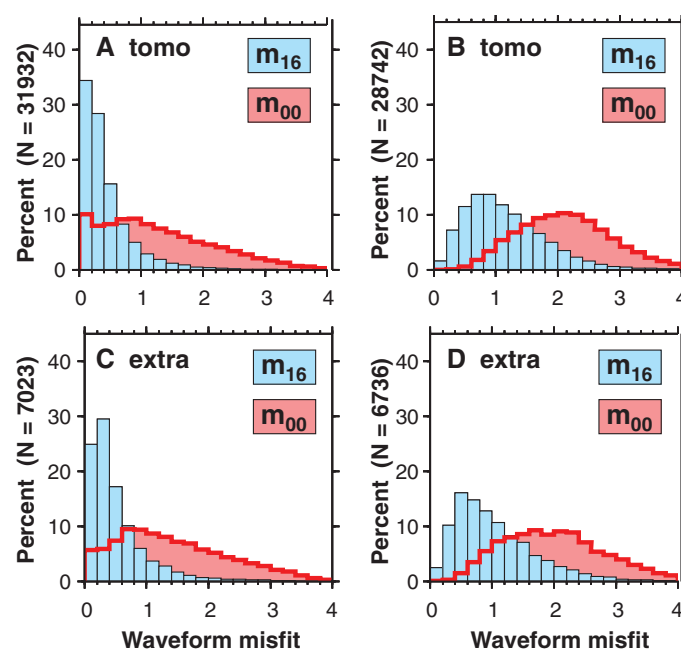
graphic model. Our inversion variables are V_S and V_B . The topography of primary interfaces (Moho and basement surface) is fixed, anisotropy is not permitted, and attenuation does not change.

We present our new crustal model on both relative and absolute scales (8). First, the update to the seismological model (the relative scale) reveals the changes to the initial SCEC model that are required by the data. We compute the update as $\ln(\mathbf{m}_{16}/\mathbf{m}_{00})$, where \mathbf{m}_{16} is the sixteenth iteration from the initial model \mathbf{m}_{00} . Second, the seismological model itself reveals the absolute model parameters (e.g., wave speed in units of km/s) and is more relevant for geologic and geodynamic interpretations. All cross sections discussed below are of V_S models (\mathbf{m}_{00} and \mathbf{m}_{16}). The V_S model is better resolved than the V_B model (fig. S9).

Figure 1 shows the iterative improvement from \mathbf{m}_{00} to \mathbf{m}_{16} of a single three-component seismogram. The initial travel-time difference (or “time shift”) for the Rayleigh wave in the 1D model is 9.60 s on the vertical component (Z) and 9.85 s on the radial component (R). In the initial SCEC model (\mathbf{m}_{00}), the Rayleigh wave time shift is 7.00 s (Z) and 7.30 s (R). After 16 iterations, the time shifts are 0.95 s (Z) and 1.00 s (R). The evolution of the transverse component is more dramatic, because there is virtually no energy between 110 s and 140 s in the SCEC model, and thus there is no time shift to identify. After 16 iterations, the time shift is 0.05 s, and the synthetic transverse-component seismogram captures the main shape of the waveform up to 130 s. Using the technique of (17), we determined that the waveform from 100 to 112 s is a wave reverberating between the surface and the Moho, whereas the waveform after 112 s is a Love wave.

The tomographic update, $\ln(\mathbf{m}_{16}/\mathbf{m}_{00})$, contains three principal features (Fig. 1A). First, there is the addition of the southern San Joaquin basin

Fig. 3. Waveform misfit analysis for the initial and final tomographic models. The analysis is performed for 143 earthquakes used in the inversion (A and B, “tomo”), as well as for 91 additional earthquakes not used in the inversion (C and D, “extra”). See expanded version in fig. S3. (A) Waveform difference misfit values (16, section S2) for windows used in the inversion. (B) Waveform difference misfit values for full seismograms containing at least one measurement window. (C and D) Same as (A) and (B), but for the set of extra earthquakes.



(22), marked as a -35% (slow) anomaly [with respect to (19)] immediately above the earthquake source. The basin resonates, influencing the Love wave observed after 112 s. Second, the V_S of the western Mojave is increased in the upper 3 km, decreased in the depth range 5 to 15 km, and increased in the depth range 18 to 26 km. Third, east of the Camp Rock fault, there is a -10% change in wave speed, probably associated with Quaternary volcanism (23, 24). Only through multiple iterations is it possible to isolate the locations and amplitudes of these changes.

Fits were also improved within the region containing the higher-resolution basin models (14). In Fig. 2, the seismic wavefield interacts with the Los Angeles and Ventura basins before reaching

station STC. The SCEC model captures the resonance, duration, and approximate amplitude of the observed seismogram, but the final 3D model is markedly better. In particular, the fits for the amplitudes are improved, even though amplitude differences are not built into the misfit function. This demonstrates that the 3D structural changes to the initial model induce additional focusing and amplification of the seismic wavefield.

Our overall assessment of the misfit reduction from the initial SCEC model to the final model is based on 12,583 different paths (such as Fig. 1) that capture 61,673 time windows for measurement (table S2). This assessment cannot be based simply on a travel-time misfit function, because there are many seismic waveforms in the final

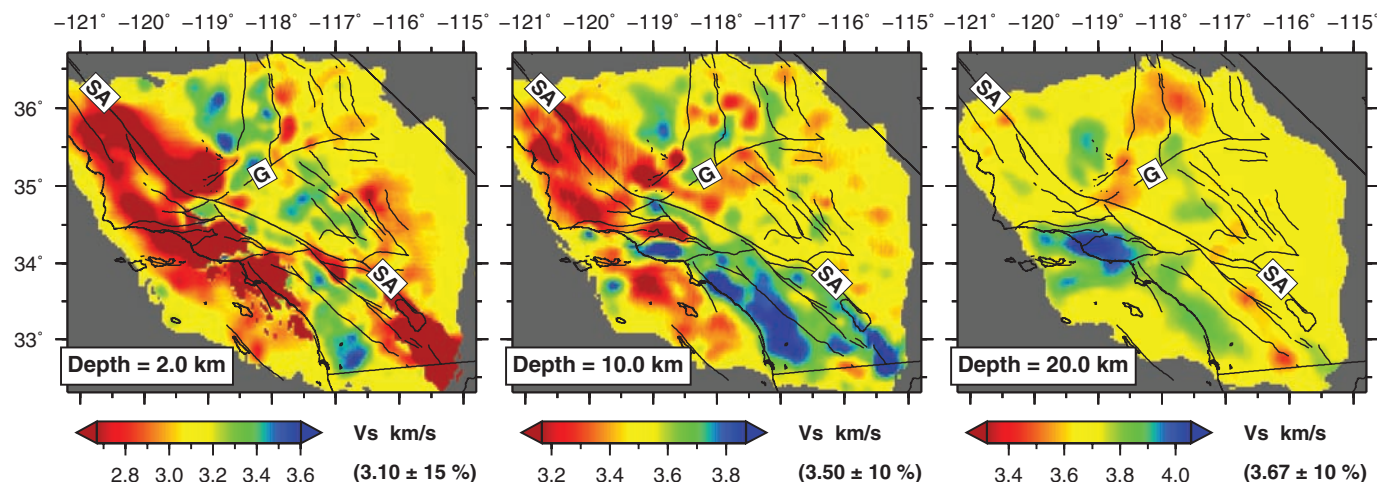


Fig. 4. Horizontal cross sections of V_5 tomographic model m_{16} at depths of 2, 10, and 20 km. See fig. S1 for locations of major features; Garlock (G) and San Andreas (SA) faults are labeled for reference.

model that do not have a measurable travel-time difference in the initial model (e.g., Fig. 1B). Thus, to facilitate a direct comparison between the two models, we compute a simple waveform difference using the time windows that were selected for the final model for the 143 earthquakes used in the tomographic inversion (Fig. 3A).

We also consider a separate set of 91 earthquakes that was not used in the tomographic inversion. An earthquake not used in the tomographic inversion—or any future earthquake, for that matter—may be used to independently assess the misfit reduction from m_{00} to m_{16} . The reduction in waveform difference misfit for the extra earthquakes is almost the same as it is for the earthquakes used in the inversion (Fig. 3). This result provides validation for the tomographic model and suggests that future earthquakes will see the same misfit reduction. We also compute waveform differences for the entire seismogram (Fig. 3, B and D), including information outside our measurement windows. We observe a reduction of misfit that is essentially the same for the two sets of earthquakes, and less than that observed for the individual windows.

The travel-time differences in the final model have a standard deviation of less than 1 s for the entire data set (fig. S4). In other words, given an adequate location, origin time, and focal mechanism for any earthquake in southern California with moment magnitude (M_w) between 3.5 and 5.5, we expect most travel-time differences computed using our crustal model to be ≤ 1 s for seismic records at periods of 2 to 30 s.

Our model shows reductions in wave speed due to both compositional and thermal features. Consider the earthquake in Fig. 1A. Above the source is the southern San Joaquin sedimentary basin (22), and east of the Camp Rock fault (25), likely related to Quaternary volcanism. West of the Camp Rock fault, slow wave speeds and high heat flow are not observed at the surface,

nor is volcanic activity. Horizontal cross sections (Fig. 4) reveal lateral variations in the new crustal model. At 2 km depth, large-scale slow (<2.8 km/s) regions show several known Neogene basins (fig. S1).

The fastest regions (>3.5 km/s) are in the Peninsular Ranges west of the Elsinore fault and in the Sierra Nevada west of the Kern Canyon fault (26). The eastern front of the Sierra Nevada is marked by an eastward step in wave speed from about 3.5 to 2.8 km/s, and the Coso geothermal region and the sedimentary fill in Owens Valley and Indian Wells Valley account for the slower wave speeds. We attribute the slow (2.9 km/s) wave speeds in the eastern Mojave to Quaternary volcanism.

At 10 km depth (Fig. 4), some of the basins are no longer visible (e.g., Los Angeles and the Salton trough), and a striking pattern of wave speeds west of the San Andreas fault is evident. The Peninsular Ranges and a mafic layer beneath the Salton trough (27) form a fast (3.8 km/s) region that is separated by the San Andreas fault from slower (3.4 km/s) regions to the northeast.

The 50-km scale variations in wave speeds along the longitudinal line 119°W illuminate, from north to south, the western Sierra Nevada (fast), the southern San Joaquin basin (slow), the San Emigdio Mountains (fast), the Ventura basin (slow), the Santa Monica Mountains (fast), and the Santa Monica basin (slow). Wave speeds in the Coast Ranges are slowest (3.1 km/s) east of the San Andreas (28) and along the coast, and are somewhat faster (3.4 km/s) in between, where Mesozoic granitic and sedimentary rocks are exposed at the surface. The northwestern Mojave is slow (3.3 km/s) compared with faster (3.6 km/s) material in the southern Sierra Nevada, across the Garlock fault.

At 20 km depth (Fig. 4), the most striking feature is the fast wave-speed (4.1 km/s) region beneath the Ventura–Santa Barbara basin and the Santa Monica Mountains, also observed in fig.

S10A. This region coincides with the surface expression of the western Transverse Ranges block (WTRB) (fig. S1), bound to the north by the Santa Ynez fault and to the south by the Malibu Coast fault. We interpret this feature as subduction-captured Farallon oceanic crust, on top of which the WTRB rotated clockwise by more than 90° from a position near the Peninsular Ranges (3.8 km/s) (29). It is possible that the WTRB crustal anomaly is related to upper-mantle anomalies observed below this region (30).

The heterogeneity in the crust (Fig. 4) strongly influences seismic wave propagation from moderate earthquakes ($M_w = 3.5$ to 5.5), such as those in this study. Using the new crustal model, we simulated the details of earthquake ground motion at periods of 2 s and longer for hundreds of different paths in southern California. By beginning to fit complex propagation paths for moderate earthquakes, we provide hope for accurately simulating larger—and damaging—earthquakes that may occur in the future (31). An improved crustal model will also enable better location of earthquakes and identification of faults. Applied at the crustal scale, spectral-element and adjoint methods provide a valuable tool for improving seismic hazard assessment.

References and Notes

1. J. H. Woodhouse, A. M. Dziewonski, *J. Geophys. Res.* **89**, 5953 (1984).
2. B. Romanowicz, *Annu. Rev. Earth Planet. Sci.* **31**, 303 (2003).
3. S. P. Grand, R. D. van der Hilst, S. Widiyantoro, *GSA Today* **7** (no. 4), 1 (1997).
4. R. Montelli *et al.*, *Science* **303**, 338 (2004).
5. A. Dziewonski, D. Anderson, *Phys Earth Planet Inter* **25**, 297 (1981).
6. D. Komatitsch, J. Ritsema, J. Tromp, *Science* **298**, 1737 (2002).
7. V. Akçelik *et al.*, *Proc. ACM/IEEE Supercomputing SC2003 Conference (SC'03)*, 15 to 21 November 2003, Phoenix, AZ.
8. P. Chen, L. Zhao, T. H. Jordan, *Bull. Seismol. Soc. Am.* **97**, 1094 (2007).
9. A. Fichtner, B. L. N. Kennett, H. Igel, H.-P. Bunge, *Geophys. J. Int.* **175**, 665 (2008).

10. A. Tarantola, *Geophysics* **49**, 1259 (1984).
11. O. Talagrand, P. Courtier, *Q. J. R. Meteorol. Soc.* **113**, 1311 (1987).
12. J. Tromp, C. Tape, Q. Liu, *Geophys. J. Int.* **160**, 195 (2005).
13. C. Tape, Q. Liu, J. Tromp, *Geophys. J. Int.* **168**, 1105 (2007).
14. M. P. Süß, J. H. Shaw, *J. Geophys. Res.* **108**, 2170 (2003).
15. D. Komatitsch et al., *Bull. Seismol. Soc. Am.* **94**, 187 (2004).
16. Additional details are available as supporting material on Science Online.
17. Q. Liu, J. Tromp, *Bull. Seismol. Soc. Am.* **96**, 2383 (2006).
18. E. Hauksson, *J. Geophys. Res.* **105**, 13875 (2000).
19. G. Lin, P. M. Shearer, E. Hauksson, C. H. Thurber, *J. Geophys. Res.* **112**, B11306 (2007).
20. T. M. Brocher, *Bull. Seismol. Soc. Am.* **95**, 2081 (2005).
21. A. Maggi, C. Tape, M. Chen, D. Chao, J. Tromp, *Geophys. J. Int.* **178**, 257 (2009).
22. E. D. Goodman, P. E. Malin, *Tectonics* **11**, 478 (1992).
23. P. Luffi, J. B. Saleeby, C.-T. A. Lee, M. N. Ducea, *J. Geophys. Res.* **114**, B03202 (2009).
24. Quaternary and Tertiary volcanic rocks lie predominantly east of the northwest-striking faults of (from north to south) Gravel Hills–Harper, Harper Lake, Camp Rock, and Emerson.
25. J. L. Bonner, D. D. Blackwell, E. T. Herrin, *Bull. Seismol. Soc. Am.* **93**, 2333 (2003).
26. N. M. Shapiro, M. Campillo, L. Stehly, M. H. Ritzwoller, *Science* **307**, 1615 (2005).
27. G. S. Fuis, W. D. Mooney, J. H. Healy, G. A. McMechan, W. J. Lutter, *J. Geophys. Res.* **89**, 1165 (1984).
28. F. Bleibinhaus, J. A. Hole, T. Ryberg, G. S. Fuis, *J. Geophys. Res.* **112**, B06315 (2007).
29. C. Nicholson, C. C. Sortien, T. Atwater, J. C. Crowell, B. P. Luyendyk, *Geology* **22**, 491 (1994).
30. E. D. Humphreys, R. W. Clayton, *J. Geophys. Res.* **95**, 19,725 (1990).
31. K. B. Olsen et al., *Geophys. Res. Lett.* **33**, L07305 (2006).
32. Seismic waveforms were provided by the Southern California Earthquake Data Center (SCEC), the Northern California Earthquake Data Center (NCEC), the Incorporated Research Institutions for Seismology (IRIS), and the University of

Nevada Reno. All earthquake simulations were performed on the CITerra Dell cluster at the Division of Geological and Planetary Sciences of the California Institute of Technology. M. Sambridge suggested using a source subspace projection method to compute the tomographic model update. We acknowledge support by the National Science Foundation under grant EAR-0711177. This research was supported by the Southern California Earthquake Center. SCEC is funded by NSF Cooperative Agreement EAR-0106924 and U.S. Geological Service Cooperative Agreement 02HQAG0008. The SCEC contribution number for this paper is 1261. The Fortran90 software packages SPECFEM3D and FLEXWIN are available for download at www.geodynamics.org.

Supporting Online Material

www.sciencemag.org/cgi/content/full/325/5943/988/DC1
SOM Text

Figs. S1 to S9
Tables S1 to S5
References

22 April 2009; accepted 29 June 2009
10.1126/science.1175298

Bacteriophages Encode Factors Required for Protection in a Symbiotic Mutualism

Kerry M. Oliver,^{1*} Patrick H. Degnan,² Martha S. Hunter,³ Nancy A. Moran²

Bacteriophages are known to carry key virulence factors for pathogenic bacteria, but their roles in symbiotic bacteria are less well understood. The heritable symbiont *Hamiltonella defensa* protects the aphid *Acyrtosiphon pisum* from attack by the parasitoid *Aphidius ervi* by killing developing wasp larvae. In a controlled genetic background, we show that a toxin-encoding bacteriophage is required to produce the protective phenotype. Phage loss occurs repeatedly in laboratory-held *H. defensa*-infected aphid clonal lines, resulting in increased susceptibility to parasitism in each instance. Our results show that these mobile genetic elements can endow a bacterial symbiont with benefits that extend to the animal host. Thus, phages vector ecologically important traits, such as defense against parasitoids, within and among symbiont and animal host lineages.

Invertebrate animals are frequently infected with heritable symbionts, which can spread and persist within host populations by providing benefits to the host organism. For example, terrestrial arthropods that feed exclusively on vertebrate blood or plant sap require nutrients supplied by microbial associates to complete dietary needs (1). Recent work has also revealed that inherited symbionts can benefit diverse invertebrate hosts by providing protection against a range of natural enemies, including pathogens, predators, and parasitoid wasps (2).

In the aphid *Acyrtosiphon pisum*, infection with the inherited gammaproteobacterial symbiont *Hamiltonella defensa* confers protection against an important natural enemy, the para-

sitoid wasp *Aphidius ervi* (3). Female wasps deposit an egg into the aphid hemocoel, which develops within the living aphid before pupating and eventually killing the aphid host (Fig. 1A). Aphids infected with *H. defensa*, however, survive and reproduce when wasps are killed before completing development (4). Bioassays have revealed that levels of protection conferred by different strains of *H. defensa* can vary substantially (5). In the absence of parasitism, *H. defensa* is not required for aphid survival and reproduction, yet surveys of aphid populations in North America and Europe have found that significant proportions of pea aphids (40 to 70%) may be infected and that a wide variety of other aphid species also carry this symbiont (4, 6–8), which appears to confer protection in aphids other than *A. pisum* (9). In experimental populations, the proportion of *H. defensa*-infected aphids increased rapidly under pressure from parasitoid wasps, indicating that defensive benefits probably contribute to the spread of *H. defensa* in natural populations (10). The proportion of infected aphids decreased in the ab-

sence of parasitism, which suggests costs to infection that limit the spread of *H. defensa* (10).

In bacteria, including some symbionts and intracellular pathogens, lateral exchange of genetic material is typically mediated by mobile genetic elements, including transposons, plasmids, and bacteriophages (11). Such elements can introduce functions that may benefit multiple partners in a symbiotic interaction when their interests are aligned (12). *H. defensa* are frequently infected with a lysogenic lamdoid bacteriophage called *A. pisum* secondary endosymbiont (APSE) (12–14). Several lines of evidence link APSE to the protective phenotype. First, variants of APSE have been identified among strains of *H. defensa*, and each encodes homologs of toxins that are known (or suspected) to target eukaryotic tissue (12, 13). For example, phage variant APSE-2 contains a homolog of cytolysin distending toxin (*cdtB*) (12), and aphids infected with APSE-2—carrying *H. defensa* are moderately protected from parasitism (~40% *A. ervi* mortality) (3, 5). APSE-3 encodes a tyrosine-aspartic acid repeat (YD-repeat)—containing protein, which also appears to be a toxin (13). Strains of *H. defensa* carrying APSE-3 were each found to confer high levels of protection (>85% *A. ervi* mortality) (5). The hypothesis that APSE and associated toxins are involved in aphid protection was bolstered by the results of a multi-locus study that found that the highly protective strains of *H. defensa* that carry APSE-3 are identical at 10 bacterial chromosomal markers to a third strain that lacks APSE and confers very little protection (5, 13).

The *H. defensa* chromosome contains virulence factors, including RTX (repeats in toxin) toxins, that could contribute additional protective mechanisms (12, 15). Therefore, despite analyses that showed a correlation between level of protection and presence of APSE, previous evidence could not exclude the hypothesis that variation on the *H. defensa* chromosome is the basis for the

¹Department of Entomology, University of Georgia, Athens, GA 30602, USA. ²Department of Ecology and Evolutionary Biology, University of Arizona, Tucson, AZ 85721, USA. ³Department of Entomology, University of Arizona, Tucson, AZ 85721, USA.

*To whom correspondence should be addressed. E-mail: kmoliver@uga.edu

Adjoint Tomography of the Southern California Crust

Carl Tape, Qinya Liu, Alessia Maggi and Jeroen Tromp

Science **325** (5943), 988-992.
DOI: 10.1126/science.1175298

Crustal Details Revealed

In seismic tomography, a large collection of data representing paths through Earth are inverted to provide an analysis of variation of density in which errors are minimized. Typically, the inversion starts with a simple layered model of the tomographic region. **Tape *et al.*** (p. 988) show how, starting with a three-dimensional model, based on synthetic seismograms, an improved iterative inversion approach can lead to a much more detailed view of a region. Using the rich data for Southern California, the model reveals details of the geologic history of the crust in this region.

ARTICLE TOOLS

<http://science.sciencemag.org/content/325/5943/988>

SUPPLEMENTARY MATERIALS

<http://science.sciencemag.org/content/suppl/2009/08/20/325.5943.988.DC1>

RELATED CONTENT

[file:/contentpending:yes](#)

REFERENCES

This article cites 27 articles, 10 of which you can access for free
<http://science.sciencemag.org/content/325/5943/988#BIBL>

PERMISSIONS

<http://www.sciencemag.org/help/reprints-and-permissions>

Use of this article is subject to the [Terms of Service](#)